

# Nonuniform heating of a substrate in evaporative lithography

M.A. Al-Muzaiqer<sup>a,b</sup>, K.S. Kolegov<sup>c,d,e</sup>, N.A. Ivanova<sup>a,b</sup>, V.M. Fliagin<sup>a,b</sup>

<sup>a</sup>*University of Tyumen, Photonics and Microfluidics Lab., X-BIO Institute, 6 Volodarskogo, Tyumen, 625003, Russia*

<sup>b</sup>*University of Tyumen, Microfiltration Processes Lab., 6 Volodarskogo, Tyumen, 625003, Russia*

<sup>c</sup>*Astrakhan State University, Mathematical Modeling Lab., 20a Tatischcheva, Astrakhan, 414056, Russia*

<sup>d</sup>*Volga State University of Water Transport, Caspian Institute of Maritime and River Transport, 6 Nikolskaya, Astrakhan, 414000, Russia.*

<sup>e</sup>*Landau Institute for Theoretical Physics Russian Academy of Sciences, 1-A Academician Semenov, Chernogolovka, 142432, Russia*

## Abstract

The work is devoted to the study of one method connected with structured sediments formation, which belongs to the direction of evaporative lithography. A series of experiments were carried out with nonuniform evaporation of an isopropanol film containing polystyrene microspheres that occurred in an open cylindrical cell. The local inhomogeneity of the vapor flux density was achieved due to the temperature gradient. A copper rod was mounted in the central part of the bottom of the cell for further heating. The thermocapillary flow resulting from the surface tension gradient due to the temperature drop transfers the particles that were originally at rest along the bottom of the cell. The effect of the initial thickness of the liquid layer on the height and area of the sediment (cluster) formed in the central region of the cell is experimentally studied. The velocity of the particles was measured using particle image velocimetry. A mathematical model describing the process at the initial stage is developed. The equations of heat transfer and thermal conductivity were used to define the temperature distribution in the liquid and the cell. The fluid flow was simulated by the lubrication approximation. The particle distribution was modeled using the convection-diffusion equation. The evaporation flux density was calculated using the Hertz-Knudsen equation. The dependence of the liquid viscosity on the particle concentration was described by Mooney's formula. Numerical results showed that the liquid film gradually becomes thinner in the central region, as the surface tension decreases with increasing temperature. The liquid flow is directed to the heater near the substrate. It transfers the particles to the center of the cell. The volume fraction of the particles increases over time in this region. The work done allowed us to formulate the conclusion that the heat flow from the heater affects the geometry of the sediment for two reasons. First, the Marangoni flow velocity depends on the temperature gradient. Secondly, the decrease in film thickness near the heater depends on the temperature.

**Keywords:** Evaporative lithography, droplets, films, colloidal liquids, microstructures, particles, Marangoni flow.

## 1. Introduction

The method of evaporative lithography consists of creating conditions for nonuniform evaporation from the free surface of a colloidal liquid [1, 2, 3]. The compensatory flow occurs due to the nonuniform evaporation of the liquid and transfers the particles to the areas of intense evaporation. It is possible to control the vapor flux density along the free surface of the liquid layer, for example, by placing a mask above a droplet [2, 4]. The resulting structures follow the shape of the holes in the masks, which play the role of templates. In the case of a predominant Marangoni flow, the precipitation structures are inverted relative to the holes in the mask [5]. External sources of airflow [6] and composite substrates with variable thermal properties [7, 8] can also be useful for evaporative lithography applications. If the melting point of the particles is higher than room temperature, the resulting precipitation is brittle. Therefore, to obtain solid relief films, heating with IR light is added to the system [9, 10, 11]. In addition, it accelerates the drying process

and the formation of a hard coating. The effect of laser heating of the droplet apex on the deposition structure of colloidal particles was compared with heating of the entire substrate in [12]. A similar experiment was performed with a drop of saline solution on hydrophobic and hydrophilic substrates [13]. The droplet heating by xenon lamp radiation leads to a more pronounced annular deposit of gold nanoparticles is formed compared to the heating of the substrate, when a part of the nanoparticles is deposited in the inner region [14]. Coffee rings formed during droplets drying on substrates at a temperature gradient were considered in the experiment [15]. It is possible to change the direction and pattern of flow due to the heating or nonuniform heating of the droplet [16]. The experiment was carried out with a drop confined between two plates of glass (Hele-Shaw cell). The local particle concentration was measured at different time points. The Marangoni flow was modeled using the stationary Navier-Stokes equations. The model takes into account thermodiffusion and heat convection. The temperature boundary conditions were specified by linear approximations. The experiment [17] showed the effect of gold nanoparticles on the evaporation rate of a drop on a heated substrate. At different substrate temperatures, an annular precipitate, a uniform

\*Corresponding authors.

Email addresses: konstantin.kolegov@asu.edu.ru (K.S. Kolegov), n.ivanova@utmn.ru (N.A. Ivanova)

spot [18], or an eye-shaped precipitate [19] can form. This is due to the competition between capillary and thermocapillary flows. It is possible to use such competition to regulate the thickness of the micro-needles that form when the polymer film dries in a heated cell near its wall [20]. The effect of the substrate temperature and the initial concentration of nanoparticles on the final sediment shape was previously studied [21]. The geometrical characteristics of drying hydrocarbon droplets and the resulting deposits on a heated aluminum substrate were analyzed in [22].

A number of papers have considered pure liquids. The theory of Marangoni flows in nonuniformly heated films was described in detail in the review [23]. The thermocapillary rupture of the film in a cell with a built-in heater was experimentally investigated in [24, 25, 26]. The kinetics of evaporation under local heating of the droplet was studied in [27]. Point heating of the substrate with a laser was carried out in the area of the center or periphery of the drop. This led to the appearance of Marangoni flows. Various thermal patterns associated with hydrothermal waves have been observed [27]. The simulation results showed that the evaporation is jointly affected by the local heating of the droplet and the wettability of the substrate [28]. An experiment with the evaporation of a drop on a heated hydrophobic substrate was carried out in [29]. An analytical solution of the stationary problem for calculating the Marangoni flow is obtained.

In the current work, we study the possibility of controlling the deposition of particles during the evaporation of a colloidal liquid using a local heater mounted in the central part of the bottom of the open cell.

## 2. Methods

### 2.1. Experiment

#### 2.1.1. Technical details

A sketch of the experimental setup is shown in Fig. 1a. The fluidic cell consists of a substrate of welding glass and glued a photopolymer ring down it (4 mm of high and an inner diameter of 20 mm). In the center of the substrate, a hole was drilled. A copper rod (the radius of  $R_h = 0.9$  mm) was hermetically fitted into the hole and connected to the heated side of the Peltier element (NEC1-00703, 10×10×4.9 mm<sup>3</sup>). As working materials, polystyrene microspheres and volatile isopropyl alcohol (isopropanol) were used. The geometrical parameters and properties of materials are summarized in Tables 1, 2 (see section 2.2.4).

The experiments were carried out according to the following procedure. Dry microparticles (15 mg) were placed onto the substrate of the experimental cell and covered with an isopropanol layer. The particles were stirred constantly with a pipette tip as long as particle distribution began to be uniform in the layer. Analysis of optical images of such initial distribution showed that particles are quite densely cover the substrate.

After starting of heating, the process of cluster formation was recorded using the microscope using the microscope Axi Zoom.V16 with the lens Zeissapo 1.5x/0.37 FWD 30 mm

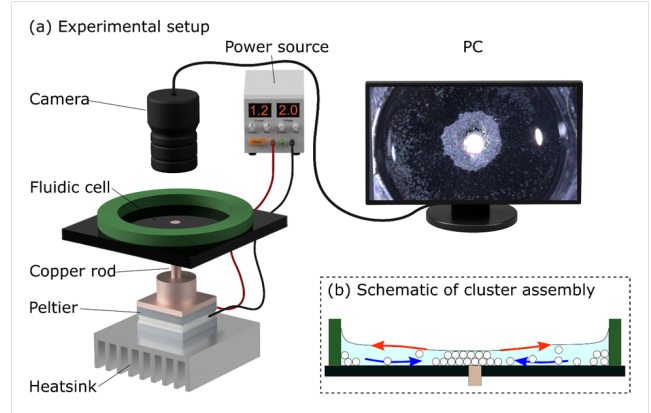


Figure 1: (a) Sketch of the experimental setup. (b) An illustration of the assembly process of the cluster in the heating zone. The outwards arrows show thermocapillary flows. The inwards arrows note reverse bottom flows to the heater.

equipped with CCD camera Zeiss Axiocam 506 color (Fig. 1a). Then the particles have formed the cluster (Fig. 1b), isopropanol continued evaporating until it disappeared. Further, the experiment is repeated again after the required volume of alcohol was added into the cell that contains the dry particles. Experiments were performed for two cases of liquid film thicknesses ( $h_0 \approx 400$  and  $700 \mu\text{m}$ ) at a constant voltage applied (+2V) to the Peltier module. To control the reproducibility, experiments were repeated five times for each layer thickness. Then the captured images analyzed and the area of the particle cluster,  $S(t)$ , forming on the substrate upon heating was measured for both values of  $h_0$ . The sediment profile,  $h_d(r)$ , was measured using the contour analysis system (OCA 15, Data-Physics Instruments). The evolution and radial distribution of temperature were measured using an IR camera (Flir A655sc, spectral range 7.5–14  $\mu\text{m}$ ,  $\pm 2^\circ\text{C}$ ).

#### 2.1.2. The cluster area estimation

During heating, the area of the particle cluster was measured using a sequence of frames. The boundary of the cluster was defined as a transition from high to low intensity of pixels. A schematic of the method for determining the boundary is shown in Fig. 2a (the colors of images are inverted to improve the perception). A central point shown by a yellow crisscross is set in the center of the growing cluster. Then, lines are drawn from this point (the red arrows in Fig. 2a) in all directions with a step of  $0.25^\circ$ . Such a small angle makes it possible to measure in detail the boundary of a cluster in an image with a resolution of 1920×1200 pixels. The length of the line is determined by the outermost particle of the cluster. We used the linear interpolation of the outer sediment boundary based on the obtained discrete values (the red outline in Fig. 2b). Then the area (the green area in Fig. 2c) enclosed by that boundary is calculated.

#### 2.1.3. Error analysis

The error in determining the cluster area is the sum of error in the calculation of the image pixels included in the calculated

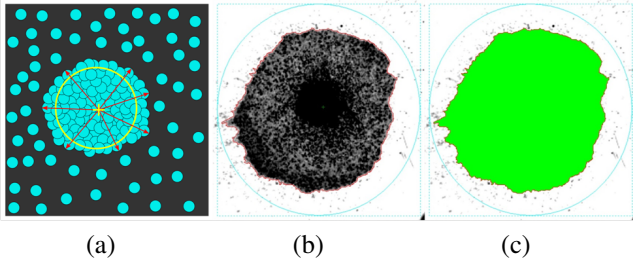


Figure 2: The method for measurement of the cluster area: (a) the schematic representation of the cluster, (b) the formation of the cluster outline (the red line), (c) the calculation of the cluster area (the green area enclosed with the red line).

area and the statistical error arising from carrying out a set of experiments upon given parameters with subsequent averaging. The first type of error in measuring the area is associated with 1) inaccuracy in determining the assembly boundary and 2) overestimation of the cluster area due to particles moving towards the center. It was found that individual particles form in the images a spot with a diameter of  $4 \pm 1$  pixels (the image scale is  $17 \mu\text{m} / \text{pixel}$ ), which means that the error in determining the position of the cluster boundary can be estimated as  $\pm 0.5$  pixel. To estimate the error in measuring the area, the cluster perimeter was measured at three moments of time after the start of heating: 20, 30, and 45 s (a stationary cluster area). Later, we analyzed other error components considering these time periods. The perimeter was calculated as the number of pixels on the cluster border. Therefore, taking into account the error in determining the position of the border, the error in the area measurement is to half the area of pixels located along the perimeter. The estimates for the considered points of time showed the maximum value of the relative error in the area measurement is at the level of  $\pm 1.4\%$ .

Overestimating the cluster area arises if the particle transferred by the flow over the stationary particles crosses the cluster boundary. In the current frame, the area of such particles is added to the total cluster area, but in the next frames, they can move above the cluster and, as a result, not increase the resulting cluster area. This error contributes at the early stages noticeably due to the small size of the forming cluster and the high intensity of convective flows at the later stages. It is possible to estimate the largest value of this error by multiplying the perimeter of the cluster by the particle radius. This value corresponds to the case of the cluster is surrounded by such particles, but some of them are just approaching the cluster boundary, and others are crossing the cluster boundary. In reality, there is a gap between moving particles no less than the particle diameter. Therefore, the estimate was corrected by dividing the perimeter in half. The maximum value of the relative error is  $\pm 5.6\%$  in this case. The final values of the error in measuring the area do not exceed  $\pm 5.8\%$ .

#### 2.1.4. Particles velocity field

The cluster assembly process is realized by the movement of microparticles to the heater. The video recording of this movement can be analyzed using particle image velocimetry

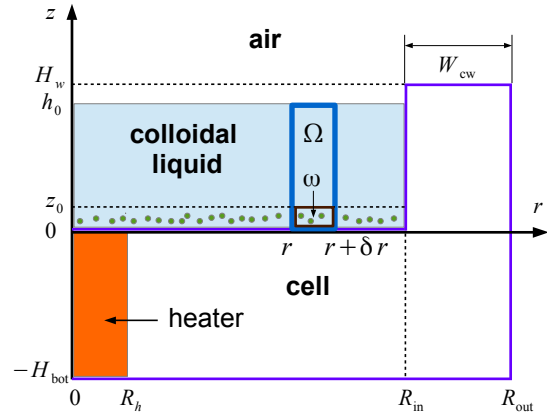


Figure 3: The domain of the problem solution.

(PIV) technology, which allows determining the particle velocity field. However, in contrast to the standard that considers a small tracer concentration, there is a huge particle number in our experiments. It increases the probability of wrong determination of their positions and the velocities as a consequence. In addition, individual particles are detected only outside the cluster, while particles moving above it are not detected against the background of non-movable particles in the cluster. It should also be noted that with the development of a thermocapillary vortex and an increase in the flow velocity, the number of particles entrained by the outward thermocapillary flow along the free surface to the wall of the cell increases. Therefore, the map of particles velocity field contains vectors directed both to and from the heater, which complicates the processing. For this reason, it is possible to obtain plausible results only for the initial stage of the particle assembly process (during 30 s from the beginning of heating).

To determine the velocity field, the video was split into frames with a frequency of 10 Hz and analyzed using the open-source software package (OpenPIV) [30]. Then, the velocity fields obtained at each point of time were processed by averaging the velocity magnitude over the radius relative to the center of the heater, with a step of 0.1 mm. We saved the obtained spatiotemporal values of the flow velocity in a two-dimensional array for further visualization.

## 2.2. Simulation

### 2.2.1. Problem statement

Let us consider a colloidal liquid in an open glass cell (Fig. 3). A heater is mounted in the center of the bottom of the cylindrical cell. We denote the inner radius of the cell as  $R_{\text{in}}$ , the radius of the mounted heating element as  $R_h$ , and the initial thickness of the colloidal film as  $h_0$ . The film is thin ( $h_0 \ll R_{\text{in}}$ ), so the vertical transfer of mass and heat is not taken into account. In addition, as the experiment showed, the particles move mainly near the substrate.

Here we focus on a qualitative description of the process, so we believe that the particle density corresponds to the density

of the liquid. In fact, the density of isopropanol is about 20% less than the density of polystyrene.

### 2.2.2. Model equations

The fluid flow velocity will be calculated using the lubrication approximation [31, 32, 33],

$$u = \frac{h}{2\eta_0} \frac{\partial\sigma}{\partial r} - \frac{h^2}{3\eta_0} \frac{\partial P}{\partial r}, \quad (1)$$

where  $h(r, t)$  is the film thickness,  $u(r, t)$  is the velocity of radial flow averaged by the film thickness,  $\eta_0$  is the dynamic viscosity of a pure liquid,  $\sigma(r, t)$  is the surface tension coefficient,  $P(r, t)$  is the capillary pressure,  $r$  and  $t$  are the space coordinate and time accordingly. With using the linear approximation  $\sigma = \sigma_0 + \sigma' \Delta T$ , we get  $\partial\sigma/\partial r = \sigma' \partial T/\partial r$ , where  $\Delta T = T_l - T_0$ ,  $T_l(r, t)$  is the liquid temperature,  $\sigma_0$  is the surface tension on the room temperature  $T_0$ , and  $\sigma' = \partial\sigma/\partial T$ . The capillary pressure  $P(r, t)$  is described by the Young–Laplace equation. Taking into account the lubrication approximation [34],

$$P = -\frac{\sigma}{r} \frac{\partial}{\partial r} \left( r \frac{\partial h}{\partial r} \right). \quad (2)$$

The formula (1) takes into account the capillary flow and the Marangoni flow. The evolution in the film thickness in space and time is described using the law of mass conservation

$$\frac{\partial h}{\partial t} + \frac{1}{r} \frac{\partial}{\partial r} (rhu(1 - \phi)) + \frac{1}{r} \frac{\partial}{\partial r} (rhU_\omega\phi) = -\frac{J}{\rho_l}, \quad (3)$$

where  $\phi(r, t)$  is the particle volume fraction averaged by the film thickness,  $\rho_l$  is the liquid density, and  $U_\omega$  is the fluid flow velocity in subdomain  $\omega$ . The vapor flux density  $J(r, t)$  is determined using the Hertz–Knudsen formula [35, 36, 37, 38, 39, 40]

$$J = \alpha_e \sqrt{\frac{M}{2\pi RT_{\text{sat}}}} (P_{\text{sat}}(T) - P_v).$$

Here,  $\alpha_e$  is the evaporation coefficient [41],  $M$  is the molar mass,  $R$  is the universal gas constant,  $T_{\text{sat}}$  is the saturation temperature,  $P_{\text{sat}}$  is the saturated vapor pressure,  $P_v$  is the partial pressure of the gas in a mixture. Let us write the flow velocity in the subdomain  $\omega$  as [42, 43]

$$U_\omega = \frac{z_0}{\eta_\omega} \frac{\partial\sigma}{\partial r} + \frac{(z_0)^2}{2\eta_\omega} \frac{\partial P}{\partial r} - \frac{z_0 h}{\eta_\omega} \frac{\partial P}{\partial r}, \quad (4)$$

where  $\eta(r, t)$  is the dynamic liquid viscosity. The dependence of the viscosity on the solution concentration is predicted by Mooney's formula [44]

$$\eta_\omega = \eta_0 \exp\left(\frac{2.5\phi_\omega}{1 - K\phi_\omega}\right),$$

where  $\phi_\omega(r, t)$  is the volume fraction of particles in the subdomain  $\omega$  and parameter  $K = 1/\phi_{\text{max}}$  ( $\phi_{\text{max}}$  is the maximum volume fraction of particles). In the calculations, we will use the value  $z_0 = d_p$ , where  $d_p$  is the diameter of the particles.

Particle transfer is described by the convection–diffusion equation

$$\frac{\partial(\phi h)}{\partial t} + \frac{1}{r} \frac{\partial(rU_\omega h\phi)}{\partial r} = \frac{D}{r} \frac{\partial}{\partial r} \left( r \frac{\partial(\phi h)}{\partial r} \right). \quad (5)$$

The equation

$$\frac{\partial(hT_l)}{\partial t} + \frac{1}{r} \frac{\partial(rhuT_l)}{\partial r} = \frac{k_l}{c_l\rho_l} \frac{1}{r} \frac{\partial}{\partial r} \left( rh \frac{\partial T_l}{\partial r} \right) + \alpha_{ls} \frac{T_s - T_l}{\rho_l c_l} - \frac{LJ}{\rho_l c_l} - \frac{JT_l}{\rho_l} \quad (6)$$

describes heat transfer in liquid, where  $k_l$  is the thermal conductivity of the liquid,  $c_l$  is the specific heat capacity,  $L$  is the heat of vaporization,  $\alpha_{ls}$  is the convective heat transfer coefficient between liquid and substrate,  $T_s(r, t)$  and  $T_l(r, t)$  are substrate and liquid temperatures averaged by the film thickness. The heat transfer equation (6) takes into account the convective heat transfer in the liquid, the thermal conductivity of the liquid, heat exchange with the substrate, and cooling due to evaporation. The evolution of the substrate temperature is described by the thermal conductivity equation

$$\frac{\partial T_s}{\partial t} = \frac{k_s}{\rho_s c_s} \frac{1}{r} \frac{\partial}{\partial r} \left( r \frac{\partial T_s}{\partial r} \right) + \frac{\alpha_{ls}}{\rho_s c_s} \frac{T_l - T_s}{H_{\text{bot}}} + \frac{q}{\rho_s c_s H_{\text{bot}}}, \quad (7)$$

where the heat flux density function of  $q = q_0 f_{\text{sh}}(r)$ . Here,  $q_0$  is the heat flux density from the heater and the smoothing function of  $f_{\text{sh}}(r) = -p_s r^2/R_{\text{in}}^2$ , where parameter of  $p_s = R_{\text{in}}/R_h$ . The equation (7) takes into account the thermal conductivity, the heat source, and the heat exchange between the substrate and the liquid.

### 2.2.3. Initial and boundary conditions

Let us write down the initial conditions of the problem

$$h(r, 0) = h_0, T_{l,s}(r, 0) = T_0, \phi(r, 0) = \phi_0, \quad (8)$$

where  $T_0$  and  $\phi_0$  are the specified constants. In (8), there is a flat film surface and the uniform distribution of the particle concentration and the liquid temperature at the time  $t = 0$ . In fact, the film is similar to the meniscus, as the cell wall is wetted with a liquid. This shape of the free surface is not taken into account here since a significant curvature of the two-phase boundary is observed far away from the heating element at  $r > 0.8R_{\text{in}}$ , while the sediment is formed in the central part of the cell.

Now we write down the boundary conditions,

$$\begin{aligned} \frac{\partial h(R_{\text{in}}, t)}{\partial r} &= 0, \quad \frac{\partial\phi(R_{\text{in}}, t)}{\partial r} = 0, \\ \frac{\partial T_{l,s}(0, t)}{\partial r} &= 0, \quad \frac{\partial T_{l,s}(R_{\text{in}}, t)}{\partial r} = 0, \\ u(0, t) &= u(R_{\text{in}}, t) = U_\omega(0, t) = U_\omega(R_{\text{in}}, t) = 0. \end{aligned} \quad (9)$$

The conditions in (9) are written from the following considerations. We take into account that the radial component of the velocity vector tends to zero near the axis of symmetry and the

wall of the cell. The other conditions at  $r = 0$  are written taking into account the axial symmetry. The transfer of particles through the wall of the cell does not occur. In addition, we do not take into account the heat exchange with the environment at the boundary  $r = R_{\text{in}}$ , since  $R_{\text{in}} \gg R_h$ . Here we consider only a special case of wetting the wall with liquid when the contact angle of  $\theta = \pi/2$ . Note that the boundary condition  $\partial h(R_{\text{in}}, t)/\partial r = \cot \theta = 0$  does not contradict the initial condition  $h(r, 0) = h_0$ .

#### 2.2.4. Problem parameters

The geometric parameters of the problem are shown in the table 1. The value  $\phi_{\text{max}}$  corresponds to the volume fraction for a random dense packing of spheres. The parameter  $\phi_0$  is given for the experiment with 30 mg of polystyrene particles per 15 mL of isopropanol.

Table 1: Geometric parameters

| Symbol                  | Parameter                | Value |
|-------------------------|--------------------------|-------|
| $d_p$ [ $\mu\text{m}$ ] | Particle diameter        | 50    |
| $h_0$ [ $\mu\text{m}$ ] | Initial film height      | 750   |
| $H_{\text{bot}}$ [mm]   | Cell bottom thickness    | 3     |
| $R_h$ [mm]              | Heater radius            | 0.6   |
| $R_{\text{in}}$ [cm]    | Inner radius of the cell | 1     |
| $\phi_0$ [-]            | Initial volume fraction  | 0.002 |
| $\phi_{\text{max}}$ [-] | Maximum volume fraction  | 0.64  |

The table 2 describes the physical parameters. The indices  $l$  and  $s$  correspond to a liquid and a solid, respectively. The value  $\alpha_e$  was experimentally measured in this paper. It turned out to be 30 times less than the value for a drop of isopropanol [45]. The particle diffusion coefficient is calculated using the Einstein formula  $D = k_B T_0 / (6\pi\eta_0 r_p)$ , where Boltzmann constant  $k_B = 1.38 \cdot 10^{-23}$  J/K and the particle radius of  $r_p = 0.5d_p$ . The value of the heat flux density  $q$  is selected approximately so that the rate of temperature growth in the central region approximately corresponds to the experimental data. The heat transfer coefficient is calculated approximately by the formula  $\alpha_{ls} = k_l / (0.5H_{\text{bot}} + 0.5h_0)$ . The rest of the information is taken from various reference books. The saturated vapor pressure was calculated using the empirical formula

$$P_{\text{sat}} = A_2 + \frac{A_1 - A_2}{1 + \exp((T_l - x_0)/\Delta_x)},$$

where the parameters of  $A_1 = -1762.65199552881$ ,  $A_2 = 503914.770838647$ ,  $x_0 = 383.243463104184$ , and  $\Delta_x = 20.494618894658$ .

#### 2.2.5. Numerical method

The system of equations (1)–(7) with initial and boundary conditions (8), (9) was solved by the finite difference method. The space derivatives were approximated by the central differences. We used a constant step in time,  $\Delta t = 0.5$  s, and space,  $\delta r = 10^{-4}$  m. The mesh convergence test was conducted. The implicit difference scheme of the first and second-order approximation in time and space, respectively, was solved by the Newton method. The work was done using a mathematical package

Table 2: Physical parameters

| Symbol                                      | Parameter                                  | Value                |
|---|--|----------------------|
| $D$ [ $\text{m}^2/\text{s}$ ]               | Particle diffusion coefficient             | $3.6 \cdot 10^{-15}$ |
| $c_l$ [ $\text{J}/(\text{kg K})$ ]          | Specific heat capacity                     | 2605                 |
| $c_s$ [ $\text{J}/(\text{kg K})$ ]          | Specific heat capacity                     | 780                  |
| $k_l$ [ $\text{W}/(\text{m K})$ ]           | Thermal conductivity                       | 0.13                 |
| $k_s$ [ $\text{W}/(\text{m K})$ ]           | Thermal conductivity                       | 0.748                |
| $L$ [ $\text{J}/\text{kg}$ ]                | Heat of vaporization                       | $75 \cdot 10^4$      |
| $M$ [ $\text{kg}/\text{mol}$ ]              | Molar mass                                 | 0.06                 |
| $P_v$ [Pa]                                  | Partial pressure of the gas in the mixture | $4.23 \cdot 10^3$    |
| $q$ [ $\text{W}/\text{m}^2$ ]               | Heat flux density                          | $10^4$               |
| $R$ [ $\text{J}/(\text{kg K})$ ]            | Universal gas constant                     | 8.31                 |
| $T_0$ [K]                                   | Room temperature                           | 300                  |
| $T_{\text{sat}}$ [K]                        | Saturation temperature                     | 355.4                |
| $\alpha_e$ [-]                              | Evaporation coefficient                    | $3.1 \cdot 10^{-5}$  |
| $\alpha_{ls}$ [ $\text{W}/(\text{K m}^2)$ ] | Heat transfer coefficient                  | 69.3                 |
| $\eta_0$ [Pa s]                             | Viscosity                                  | $2.43 \cdot 10^{-3}$ |
| $\rho_l$ [ $\text{kg}/\text{m}^3$ ]         | Liquid density                             | 786                  |
| $\rho_s$ [ $\text{kg}/\text{m}^3$ ]         | Substrate density                          | 2500                 |
| $\sigma'$ [ $\text{N}/(\text{m K})$ ]       | $\sigma' = \partial\sigma/\partial T$      | $-8 \cdot 10^{-5}$   |
| $\sigma_0$ [N/m]                            | Surface tension                            | $22 \cdot 10^{-3}$   |

Maple 2019. Unfortunately, the numerical implementation allowed us to simulate the process only at the initial stage. We were able to perform the calculation up to the time  $t = 27$  s. Then, in time, there is a numerical instability. Most likely, this is due to a small value of the diffusion coefficient  $D$  and, as a consequence, a large concentration gradient  $\phi$ . A similar difficulty has occurred before in another work at using a different numerical method and software [46].

### 3. Results and discussion

#### 3.1. Experimental results

Figure 4f shows the evolution of the cluster area in the layers of 400 and 700  $\mu\text{m}$  thick. The cluster area is smaller in the case of a thick layer compared to a thin layer which agrees with the trend found in our previous study for a small particle number [47]. Figure 4b shows the distribution of the cluster height for both layers. The surface profiles were obtained by the contouring of side-view images of the cluster. The cluster is higher in the case of the 700  $\mu\text{m}$  layer. Consequently, multilayer assemblies are formed in relatively thick layers. The reason for that is the particle is uprising onto the cluster by the action of upward flows at the liquid-sediment boundary [47]. It is notable that the time the cluster was formed, i.e., the assembly time of all particles in the heating spot is the same for both thicknesses of the layer.

Figure 5 shows the velocity of particles entrained by the reverse bottom flow of liquid towards the heater. The direction from the heater center to the wall of the cell is chosen for the positive direction of the axis  $r$ . The maximum values of the velocity are achieved near the boundary of the growing cluster.

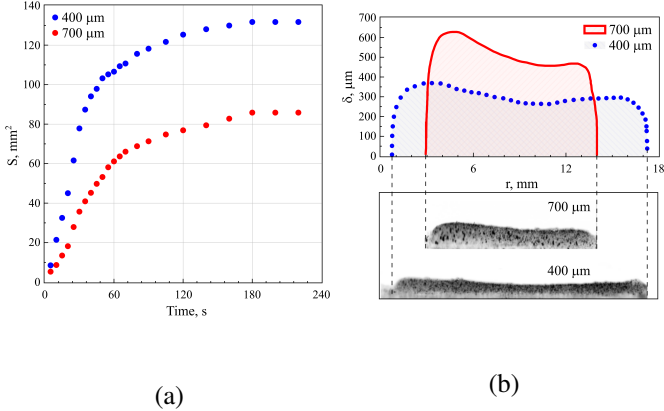


Figure 4: (a) The dependency of the cluster area on heating time at the layer thicknesses of 400 and 700  $\mu\text{m}$ . (b) Top: the height of the cluster versus its diameter (the real scale). Bottom: side view images of the cluster for both layer thicknesses; the vertical scale of images is increased two times relative to the initial images.

This is obviously associated with an increase in the temperature gradient near the boundary compared to the periphery and, as a consequence, an increase in the flow velocity.

Interestingly also that the value of the maximum particle velocity increases with the heating time and the cluster area (Fig. 5). This effect is caused by two mechanisms: an increase in the temperature difference between the cluster edge and the wall (Fig. 6a), which leads to an increase in velocity, and the formation of a small ring-like zone near the cluster boundary, which eventually becomes relatively free of particles (Fig. 6b), allowing particles to move freely in the flow without collisions or deceleration. The broadening of the averaged velocity profile over time in the 700  $\mu\text{m}$  layer (Fig. 4b) is explained by the fact that the cluster boundary on that case is asymmetric in shape compared to the 400  $\mu\text{m}$  layer.

### 3.2. Simulation results

The results of numerical calculations allow us to demonstrate the evolution in space and time of the film thickness (Fig. 7), the particle concentration (Fig. 8), the temperature of the liquid (Fig. 9) and the substrate (Fig. 10), the average velocity (Fig. 11) and the velocity of the liquid flow near the substrate (Fig. 12) at the initial stage of the process. At the initial time, the free surface of the liquid is flat. But later in time, it begins to be curved. The film bends down in the central area of the cell and rises slightly near the wall (Fig. 7). This happens for two reasons. First, in the central region, due to heating, the surface tension of the liquid decreases. Secondly, as the temperature increases, the evaporation rate increases too. This precedes the thermocapillary rupture of the film, which should occur later in time. The film thickness  $h$  decreases by about 13% in the central region of the cell during the heating time  $t = 27$  s.

The decrease of the liquid volume in the area of the heater and the mass transfer by the flow leads to an increase of the volume fraction of the particles  $\phi$ . In a relatively short period of time, the value of  $\phi$  has increased by almost an order of magnitude compared to  $\phi_0$  in the central area of the cell (Fig. 8).

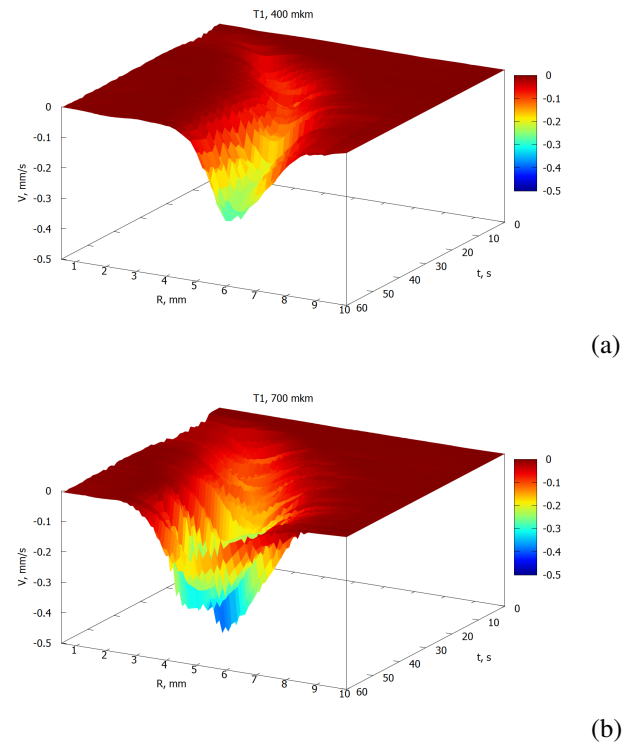


Figure 5: Particle velocity towards the heater in layers of 400  $\mu\text{m}$  (a) and 700  $\mu\text{m}$  (b).

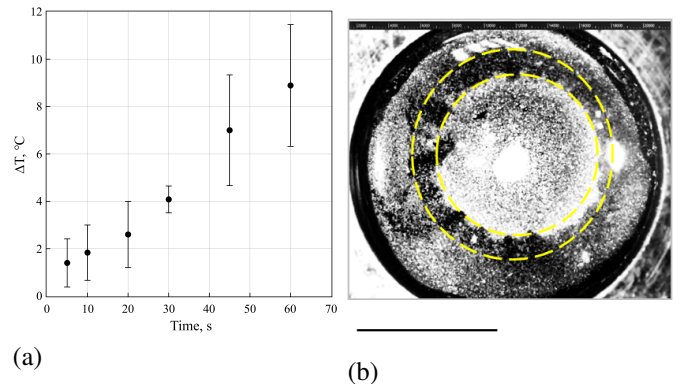


Figure 6: (a) Evolution of the temperature difference between the cluster edge and the wall. (b) A snapshot of the cluster assembly process ( $t = 24$  s) in the layer of 400  $\mu\text{m}$ . The area bounded by the two rings is marked with dashed lines. The scale bar is 5 mm.

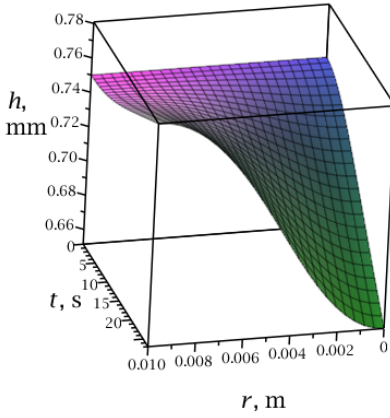


Figure 7: Dynamics of film thickness.

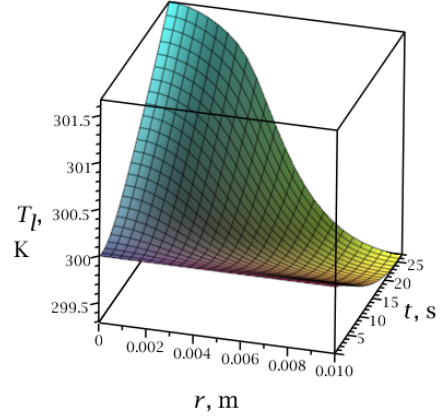


Figure 9: Fluid temperature dynamics.

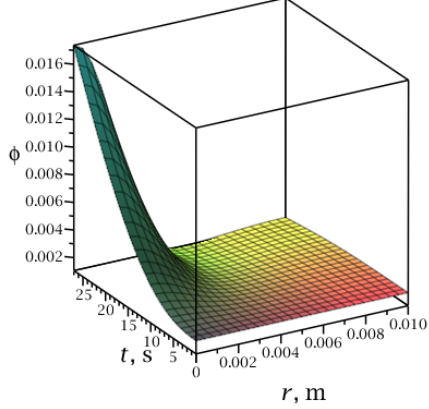


Figure 8: Dynamics of the volume fraction of particles.

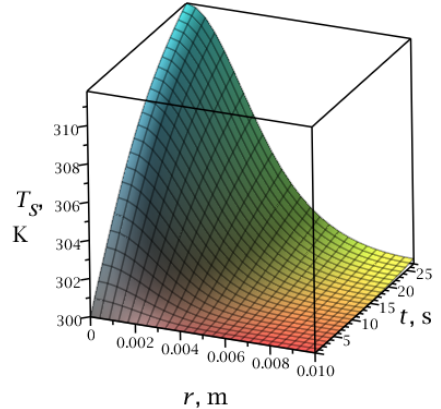


Figure 10: Dynamics of the substrate temperature.

Peclet number  $\text{Pe}_\phi = U_{\max} R_{\text{in}} / D \approx 3 \cdot 10^9$ , where characteristic velocity  $U_{\max} \approx 1 \text{ mm/s}$  according to experimental measurements. At such value of solutal Peclet number,  $\text{Pe}_\phi \gg 1$ , convective mass transfer prevails over diffusion. The diffusion term in the equation (5) is taken into account solely for reasons of computational stability.

The temperature of the liquid and the substrate increases over time, especially intensively in the central part of the cell (Fig. 9, 10). In the considered time interval, the temperature of the substrate  $T_s$  in the area of the heating element increased by 12 K. While near the wall of the cell, the temperature of  $T_s$  has not changed much. This is due to the long relaxation time of the heat in the substrate,  $t_{rs} = \pi R_{\text{in}}^2 / \chi_s \approx 819 \text{ s}$ , where the thermal diffusivity  $\chi_s = k_s / (c_s \rho_s) \text{ m}^2/\text{s}$ . In addition, there is a constant transfer of heat from the bottom of the cell (substrate) to the liquid, since  $T_s > T_l$  for any value of  $r$  at  $t > 0$ . Thermal Peclet number  $\text{Pe}_T = u_{\max} R_{\text{in}} / \chi_l \approx 1.6$ , where the thermal diffusivity  $\chi_l = k_l / (c_l \rho_l) \text{ m}^2/\text{s}$ . The maximum value of the average velocity is taken from the results of our calculations,  $u_{\max} \approx 10^{-5} \text{ m/s}$ . This value of the Peclet number,  $\text{Pe}_T$ , indicates that thermal diffusion and convection are equally important for heat distri-

bution. During this time of heating ( $t = 27 \text{ s}$ ), the temperature of the liquid in the central part of the cell increases by about 1.7 K. Near the wall,  $T_l$  decreases by about 0.7 K. It is associated with evaporation since the molecules with the highest kinetic energy leave the liquid surface and pass into the vapor phase. During this period of time, convection and thermal diffusion do not yet have time to compensate for this cooling. The temperature difference at the opposite boundaries of the calculated domain  $\Delta T_l \approx 2.4 \text{ K}$ . Thus, the appearance of the flow is affected not only by the deviation of the free surface of the film from the equilibrium shape but also by the gradient of the surface tension that occurs due to the nonuniform temperature  $T_l$ .

The radial flow velocity  $u$  averaged over the thickness of the liquid layer increases from 0 to  $10^{-5} \text{ m/s}$  over the considered time interval. The positive velocity sign indicates that the fluid transfer occurs from the center to the wall of the cell. This is due to the action of capillary forces and the change in the equilibrium shape of the film when a surface tension gradient occurs. Due to the increase in temperature, the value of  $\sigma$  decreases in the central part of the cell. Thus, the thermocapillary flow of

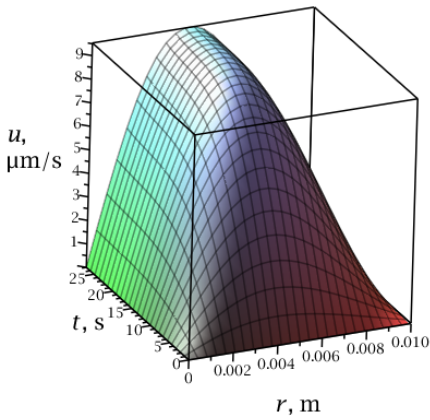


Figure 11: Dynamics of the fluid flow velocity averaged by the thickness of the liquid layer.

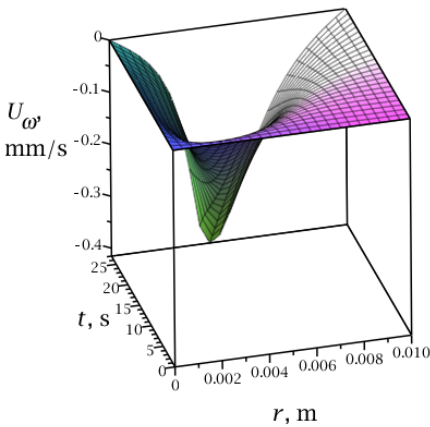


Figure 12: Dynamics of the fluid flow velocity near the substrate.

liquid along the free surface will be directed from the center to the wall of the cell to the area of a higher value of the surface tension. Near the substrate, the liquid flow is directed and transferred the particles to the central region ( $U_\omega < 0$ ). The largest values of  $u$  and  $U_\omega$  in the plots (Fig. 11, 12) are observed in the region of  $r \approx 4$  mm, where a relatively sharp drop in temperature  $T_l$  begins in the direction of the wall. The peak velocity of  $U_\omega \approx -0.4$  mm/s, which corresponds in order of magnitude to the experimental results. The opposite signs of the values  $U_\omega$  and  $u$  indicate that the flow near the free surface is more rapid than near the substrate. The obtained numerical results are in qualitative agreement with the results of the performed experiments.

#### 4. Conclusion

Evaporative lithography is a promising field that is useful for microelectronics, nanotechnology, medicine, and so on. Controlling the particle deposition and the structure formation with the required geometry and morphology on solid substrates is

one of the key problems in technologies for creating materials and coatings with various functional properties. Here we study the process of the sediment (particle cluster) formation of polystyrene microparticles distributed on a substrate under a layer of evaporating liquid (isopropanol), controlled by a point heater mounted in the center of the substrate. Local heating creates a thermocapillary flow in the liquid layer, which is directed along the free surface from the heater to the wall of the cell (from the region of low to the region of high surface tension). The inward flow near the substrate, due to the viscous friction of the liquid, creates a force acting on the particles, which leads to the transfer of the particles to the heater area. As a result of nonuniform evaporation, the particles are accumulated in a cluster in the center of the cell. Experiments have shown that the size of the cluster at a constant power of the heat source depends on the thickness of the liquid layer. An increase in the layer thickness leads to a decrease in the area of the substrate occupied by the cluster. This indicates that a multilayer particle deposit is formed in the thick layer. Therefore, It is possible to control not only the cluster area but also the number of particle layers. Using PIV method, it was established that the maximum values of the particle velocity are reached near the boundary of the growing cluster and increase with the temperature gradient. A mathematical model based on the lubrication approximation is developed. The model allows us to describe the spatiotemporal evolution in the thickness of the liquid layer, the particle concentration, the temperature of the liquid and the substrate, as well as the flow velocity near the substrate. The obtained numerical results are in qualitative agreement with the experimental results. The work done allowed us to formulate the conclusion that the heat flow from the heater affects the geometry of the sediment for two reasons. First, the Marangoni flow velocity depends on the temperature gradient. Secondly, the decrease in film thickness near the heater depends on the temperature.

#### 5. Acknowledgement

Part of the work related to mathematical modeling was supported by the grant 18-71-10061 from the Russian Science Foundation (K.S.K.). The experimental part of the research was supported by the Ministry of Science and Higher Education of the Russian Federation as part of World-class Research Center program: “Advanced Digital Technologies”, contract no. 075-15-2020-935 (M.A.Al-M., N.A.I., V.M.F.).

- [1] A. F. Routh, W. B. Russel, Horizontal drying fronts during solvent evaporation from latex films, *AIChE Journal* 44 (9) (1998) 2088–2098. [doi: 10.1002/aic.690440916](https://doi.org/10.1002/aic.690440916).
- [2] D. J. Harris, H. Hu, J. C. Conrad, J. A. Lewis, Patterning colloidal films via evaporative lithography, *Physical Review Letters* 98 (14) (2007) 148301. [doi:10.1103/PhysRevLett.98.148301](https://doi.org/10.1103/PhysRevLett.98.148301).
- [3] K. S. Kolegov, L. Y. Barash, Applying droplets and films in evaporative lithography, *Advances in Colloid and Interface Science* 285 (2020) 102271. [doi:10.1016/j.cis.2020.102271](https://doi.org/10.1016/j.cis.2020.102271).
- [4] I. V. Vodolazskaya, Y. Y. Tarasevich, Modeling of mass transfer in a film of solution evaporating under the mask with holes, *The European Physical Journal E* 40 (10). [doi:10.1140/epje/i2017-11574-8](https://doi.org/10.1140/epje/i2017-11574-8).
- [5] D. J. Harris, J. A. Lewis, Marangoni effects on evaporative lithographic patterning of colloidal films, *Langmuir* 24 (8) (2008) 3681–3685. [doi: 10.1021/la8000637](https://doi.org/10.1021/la8000637).

[6] Q. Yang, Y. Gao, F. He, P. Hao, Patterning in colloidal droplets by forced airflow, *Journal of Applied Physics* 129 (2) (2021) 024701. [doi:10.1063/5.0026182](https://doi.org/10.1063/5.0026182).

[7] P. Cavadini, J. Krenn, P. Scharfer, W. Schabel, Investigation of surface deformation during drying of thin polymer films due to marangoni convection, *Chemical Engineering and Processing: Process Intensification* 64 (2013) 24–30. [doi:10.1016/j.cep.2012.11.008](https://doi.org/10.1016/j.cep.2012.11.008).

[8] P. Cavadini, J. Erz, D. Sachsenheimer, A. Kowalczyk, N. Willenbacher, P. Scharfer, W. Schabel, Investigation of the flow field in thin polymer films due to inhomogeneous drying, *Journal of Coatings Technology and Research* 12 (5) (2015) 921–926. [doi:10.1007/s11998-015-9725-9](https://doi.org/10.1007/s11998-015-9725-9).

[9] A. Georgiadis, A. F. Routh, M. W. Murray, J. L. Keddie, Bespoke periodic topography in hard polymer films by infrared radiation-assisted evaporative lithography, *Soft Matter* 7 (2011) 11098–11102. [doi:10.1039/C1SM06527K](https://doi.org/10.1039/C1SM06527K).

[10] A. Georgiadis, F. N. Muhamad, A. Utgenannt, J. L. Keddie, Aesthetically textured, hard latex coatings by fast IR-assisted evaporative lithography, *Progress in Organic Coatings* 76 (12) (2013) 1786–1791. [doi:10.1016/j.porgcoat.2013.05.017](https://doi.org/10.1016/j.porgcoat.2013.05.017).

[11] K. S. Kolegov, Simulation of patterned glass film formation in the evaporating colloidal liquid under IR heating, *Microgravity Science and Technology* 30 (1-2) (2018) 113–120. [doi:10.1007/s12217-017-9587-0](https://doi.org/10.1007/s12217-017-9587-0).

[12] T. M. Yen, X. Fu, T. Wei, R. U. Nayak, Y. Shi, Y.-H. Lo, Reversing coffee-ring effect by laser-induced differential evaporation, *Scientific Reports* 8 (1) (2018) 3157. [doi:10.1038/s41598-018-20581-0](https://doi.org/10.1038/s41598-018-20581-0).

[13] Z. Liu, Y. Yan, X. Wang, X. Chen, Droplet deposition pattern affected by different heating directions, *Journal of Bionic Engineering* 17 (4) (2020) 795–801. [doi:10.1007/s42235-020-0058-8](https://doi.org/10.1007/s42235-020-0058-8).

[14] X. Yan, J. Xu, Z. Meng, J. Xie, A comprehensive comparison between substrate heating and light heating induced nanofluid droplet evaporation, *Applied Thermal Engineering* 175 (2020) 115389. [doi:10.1016/j.applthermaleng.2020.115389](https://doi.org/10.1016/j.applthermaleng.2020.115389).

[15] L. K. Malla, R. Bhardwaj, A. Neild, Colloidal deposit of an evaporating sessile droplet on a non-uniformly heated substrate, *Colloids and Surfaces A: Physicochemical and Engineering Aspects* (2019) 124009 [doi:10.1016/j.colsurfa.2019.124009](https://doi.org/10.1016/j.colsurfa.2019.124009).

[16] A. K. Thokchom, S. K. Majumder, A. Singh, Internal fluid motion and particle transport in externally heated sessile droplets, *AIChE Journal* 62 (4) (2015) 1308–1321. [doi:10.1002/aic.15098](https://doi.org/10.1002/aic.15098).

[17] I. Zaaroura, S. Harmand, J. Carlier, M. Toubal, A. Fasquelle, B. Non-gaillard, Experimental studies on evaporation kinetics of gold nanofluid droplets: Influence of nanoparticle sizes and coating on thermal performance, *Applied Thermal Engineering* 183 (2021) 116180. [doi:10.1016/j.applthermaleng.2020.116180](https://doi.org/10.1016/j.applthermaleng.2020.116180).

[18] H. Lama, D. K. Satapathy, M. G. Basavaraj, Modulation of central depletion zone in evaporated sessile drops via substrate heating, *Langmuir* 36 (17) (2020) 4737–4744. [doi:10.1021/acs.langmuir.0c00785](https://doi.org/10.1021/acs.langmuir.0c00785).

[19] Y. Li, C. Lv, Z. Li, D. Quéré, Q. Zheng, From coffee rings to coffee eyes, *Soft Matter* 11 (23) (2015) 4669–4673. [doi:10.1039/c5sm00654f](https://doi.org/10.1039/c5sm00654f).

[20] I. Mansoor, B. Stoeber, PIV measurements of flow in drying polymer solutions during solvent casting, *Experiments in Fluids* 50 (5) (2011) 1409–1420. [doi:10.1007/s00348-010-1000-3](https://doi.org/10.1007/s00348-010-1000-3).

[21] B. Liu, S. Wang, L. Chai, G. E. Achkar, A. Chen, P. E. Theodorakis, Experimental investigation of nanoparticles distribution mechanisms and deposition patterns during nanofluid droplet evaporation, *The European Physical Journal Applied Physics* 92 (1) (2020) 11101. [doi:10.1051/epjap/2020200168](https://doi.org/10.1051/epjap/2020200168).

[22] P. Hänichen, A. Bender, B. Voß, T. Gambaryan-Roisman, P. Stephan, Drop evaporation of hydrocarbon fluids with deposit formation, *International Journal of Heat and Mass Transfer* 128 (2019) 115–124. [doi:10.1016/j.ijheatmasstransfer.2018.08.102](https://doi.org/10.1016/j.ijheatmasstransfer.2018.08.102).

[23] T. Gambaryan-Roisman, Modulation of Marangoni convection in liquid films, *Advances in Colloid and Interface Science* 222 (2015) 319–331. [doi:10.1016/j.cis.2015.02.003](https://doi.org/10.1016/j.cis.2015.02.003).

[24] S. Spesivtsev, Y. Lyulin, Evolution of the deformation profile of a horizontal thin ethanol layer when heated locally, *MATEC Web of Conferences* 92 (2016) 01024. [doi:10.1051/matecconf/20179201024](https://doi.org/10.1051/matecconf/20179201024).

[25] D. Y. Kochkin, D. V. Zaitsev, O. A. Kabov, Thermocapillary rupture and contact line dynamics in the heated liquid layers, *Interfacial Phenomena and Heat Transfer* 8 (1) (2020) 1–9. [doi:10.1615/interfacphenomheattransfer.2020033129](https://doi.org/10.1615/interfacphenomheattransfer.2020033129).

[26] D. Y. Kochkin, D. V. Zaitsev, A. S. Mungalov, O. A. Kabov, Experimental study of the thermocapillary rupture dynamics of water and ethanol layers, *Journal of Physics: Conference Series* 1677 (2020) 012137. [doi:10.1088/1742-6596/1677/1/012137](https://doi.org/10.1088/1742-6596/1677/1/012137).

[27] A. Askounis, Y. Kita, M. Kohno, Y. Takata, V. Koutsos, K. Sefiane, Influence of local heating on Marangoni flows and evaporation kinetics of pure water drops, *Langmuir* 33 (23) (2017) 5666–5674. [doi:10.1021/acs.langmuir.7b00957](https://doi.org/10.1021/acs.langmuir.7b00957).

[28] L. Wang, Z. Liu, X. Wang, Y. Yan, Investigation on the droplet evaporation process on local heated substrates with different wettability, *Heat and Mass Transfer* [doi:10.1007/s00231-020-03005-6](https://doi.org/10.1007/s00231-020-03005-6).

[29] D. Tam, V. von Arnim, G. H. McKinley, A. Hosoi, Marangoni convection in droplets on superhydrophobic surfaces, *Journal of Fluid Mechanics* 624 (2009) 101–123. [doi:10.1017/s0022112008005053](https://doi.org/10.1017/s0022112008005053).

[30] H. Ben-Gida, R. Gurka, A. Liberzon, OpenPIV-MATLAB — an open-source software for particle image velocimetry; test case: Birds' aerodynamics, *SoftwareX* 12 (2020) 100585. [doi:10.1016/j.softx.2020.100585](https://doi.org/10.1016/j.softx.2020.100585).

[31] E. Sultan, A. Boudaoud, M. B. Amar, Evaporation of a thin film: diffusion of the vapour and Marangoni instabilities, *Journal of Fluid Mechanics* 543 (1) (2005) 183. [doi:10.1017/s0022112005006348](https://doi.org/10.1017/s0022112005006348).

[32] M. Yamamura, T. Uchinomiya, Y. Mawatari, H. Kage, Drying-induced surface roughening of polymeric coating under periodic air blowing, *AIChE Journal* 55 (7) (2009) 1648–1658. [doi:10.1002/aic.11783](https://doi.org/10.1002/aic.11783).

[33] A.-M. Cazabat, G. Guena, Evaporation of macroscopic sessile droplets, *Soft Matter* 6 (2010) 2591–2612. [doi:10.1039/B924477H](https://doi.org/10.1039/B924477H).

[34] B. J. Fischer, Particle convection in an evaporating colloidal droplet, *Langmuir* 18 (1) (2002) 60–67. [doi:10.1021/la015518a](https://doi.org/10.1021/la015518a).

[35] E. J. Davis, R. Chang, B. D. Pethica, *Interfacial temperatures and evaporation coefficients with jet tensimetry*, *Ind. Eng. Chem. Fund.* 14 (1) (1975) 27–33. [doi:10.1021/i160053a005](https://doi.org/10.1021/i160053a005). URL <https://doi.org/10.1021/i160053a005>

[36] S. Semenov, V. M. Starov, R. G. Rubio, Evaporation of pinned sessile microdroplets of water on a highly heat-conductive substrate: computer simulations, *The European Physical Journal Special Topics* 219 (1) (2013) 143–154. [doi:10.1140/epjst/e2013-01789-y](https://doi.org/10.1140/epjst/e2013-01789-y).

[37] A. H. Persad, C. A. Ward, Expressions for the evaporation and condensation coefficients in the Hertz-Knudsen relation, *Chem. Rev.* 116 (14) (2016) 7727–7767. [doi:10.1021/acs.chemrev.5b00511](https://doi.org/10.1021/acs.chemrev.5b00511). URL <https://doi.org/10.1021/acs.chemrev.5b00511>

[38] V. B. Bekezhanova, O. N. Goncharova, *Problems of evaporative convection (review)*, *Fluid Dynamics* 53 (1) (2018) S69–S102. URL <https://doi.org/10.1134/S001546281804016X>

[39] A. Zigelman, M. Abo Jabal, O. Manor, *Analysis of the oscillatory wetting-dewetting motion of a volatile drop during the deposition of polymer on a solid substrate*, *Soft Matter* 15 (2019) 3580–3587. [doi:10.1039/C9SM00192A](https://doi.org/10.1039/C9SM00192A). URL <http://dx.doi.org/10.1039/C9SM00192A>

[40] Y. Zhang, Y.-R. Li, J.-J. Yu, Q.-S. Liu, Three-dimensional numerical simulation on marangoni convection in a sessile water droplet evaporating in its vapor at low pressure, *Microgravity Science and Technology* 31 (2) (2019) 231–240. [doi:10.1007/s12217-019-9694-1](https://doi.org/10.1007/s12217-019-9694-1).

[41] D. N. Gerasimov, E. I. Yurin, *Kinetics of evaporation*, Springer International Publishing, 2018. [doi:10.1007/978-3-319-96304-4](https://doi.org/10.1007/978-3-319-96304-4).

[42] I. V. Marchuk, Thermocapillary deformation of a thin locally heated horizontal liquid layer, *Journal of Engineering Thermophysics* 18 (3) (2009) 227–237. [doi:10.1134/s1810232809030047](https://doi.org/10.1134/s1810232809030047).

[43] R. T. van Gaalen, C. Diddens, H. M. A. Wijshoff, J. G. M. Kuerten, Marangoni circulation in evaporating droplets in the presence of soluble surfactants, *Journal of Colloid and Interface Science* 584 (2021) 622–633. [doi:10.1016/j.jcis.2020.10.057](https://doi.org/10.1016/j.jcis.2020.10.057).

[44] M. Mooney, The viscosity of a concentrated suspension of spherical particles, *Journal of Colloid Science* 6 (2) (1951) 162 – 170. [doi:https://doi.org/10.1016/0095-8522\(51\)90036-0](https://doi.org/10.1016/0095-8522(51)90036-0).

[45] N. Murisic, L. Kondic, On evaporation of sessile drops with moving contact lines, *Journal of Fluid Mechanics* 679 (2011) 219–246. [doi:10.1017/jfm.2011.133](https://doi.org/10.1017/jfm.2011.133).

[46] J. A. Vieyra Salas, J. M. van der Veen, J. J. Michels, A. A. Darhuber, Active control of evaporative solution deposition by modulated infrared illumination, *The Journal of Physical Chemistry C* 116 (22) (2012) 12038–12047. [doi:10.1021/jp301092y](https://doi.org/10.1021/jp301092y).

[47] M. A. Al-Muzaiqer, N. A. Ivanova, V. M. Fliajin, P. V. Lebedev-Stepanov, Transport and assembling microparticles via Marangoni flows in heating and cooling modes, *Colloids and Surfaces A: Physicochemical and Engineering Aspects* 621 (2021) 126550. [doi:10.1016/j.colsurfa.2021.126550](https://doi.org/10.1016/j.colsurfa.2021.126550).